

Master Thesis

Sea ice effect on the Labrador Sea freshwater fluxes by (sub)mesoscale activity

Boris Shapkin

Ocean and Climate Physics

Matr.-Nr.: 7484910

First Supervisor: Prof. Dr. Eleanor Frajka-Williams

Second Supervisor: Dr. Louis Clement

Abstract

The formation of fresh, cold, oxygenated and carbon dioxide-rich Labrador Sea Water is a critical process which affects global climate by ventilating the deep ocean. Understanding the mechanisms that control the convection and generation of deep water in the Labrador Sea remains crucial. This study employs a high-resolution numerical simulation run of the Massachusetts Institute of Technology general circulation model to examine how sea ice changes affect freshwater fluxes in the Labrador Sea, primarily via (sub)mesoscale activity in the Labrador Current region. Sea ice is a thermally-insulating barrier, limiting the heat exchange between the ocean and the atmosphere. Consequently, a decrease in ocean heat loss results in shallower mixed layer depth, leading to a lower depth penetration of submesoscale instabilities. In addition, the highly-consolidated sea ice greatly suppresses the intensity of eddy activity. Our results indicate that (sub)mesoscale dynamics likely play an important role in freshwater intrusions into the deep convection region. With the future reduction of sea ice under a changing climate, the Labrador Current region might become an essential source of freshwater to the open Labrador Sea, which could influence or even stop deep convection and Labrador Sea Water formation.

Contents

Abstract	i
1 Introduction	1
2 Data & Methods	5
3 Results	10
4 Conclusion	24
References	26

1

Introduction

The Labrador Sea is a basin of the North Atlantic ocean located between Canada and Greenland. This is one of the main locations in the northern hemisphere where deep mixing of water column (convection) regularly takes place. Deep convection in the Labrador Sea causes the mixing of surface waters to depths down to 2000 meters. The result of convection is the formation of a fresh, cold and highly oxygenated water mass, mainly known as Labrador Sea Water (LSW). LSW is then carried southward across the northwest Atlantic at mid-depths (Lazier et al., 2002; Yashayaev et al., 2007).

Previous studies (e.g., Bailey et al., 2005) have indicated that LSW plays an important role in the variability and strength of the Atlantic Meridional Overturning Circulation (AMOC) - the complex, three-dimensional system of ocean currents that plays a vital role in the Earth's climate by absorbing and distributing heat and other climate-influencing properties. However, according to the recent 21-month study from the Overturning in the Subpolar North Atlantic Program (OSNAP) observing system, the eastern sub-polar gyre, rather than the Labrador Sea, determine the strength of the overturning in the sub-polar North Atlantic (Lozier et al., 2019).

Although the Labrador Sea may not significantly impact AMOC variability, the formation of LSW remains a vital process for deep ocean ventilation. LSW transports heat, nutrients, oxygen, and carbon dioxide from the surface layers to the deep ocean (Rhein et al., 2017). It remains essential to comprehend mechanisms that govern the convection and deep water formation in the Labrador Sea.

The surface circulation in the Labrador Sea is cyclonic and intensified along the

boundaries (Fig. 1.1). The water columns tend to follow f/H contours, where f is the Coriolis parameter and H is the bottom depth. The West Greenland Current (WGC) transports cold and fresh water from the Nordic Seas northwestward along the Greenland coast. The Labrador Current (LC) carries cold and low salinity water southeastward from Baffin Bay towards Nova Scotia along the western boundaries of the Labrador Sea. The LC has lower salinity than the WGC due to a direct connection with the Arctic Ocean and its freshwater outflow. Below and offshore the WGC, the Irminger Current carries warmer and saltier Irminger Sea Water over continental slopes (Cuny et al., 2002). The central basin of the Labrador Sea has a weak mean circulation but strong eddy activity (Lilly et al., 2003).

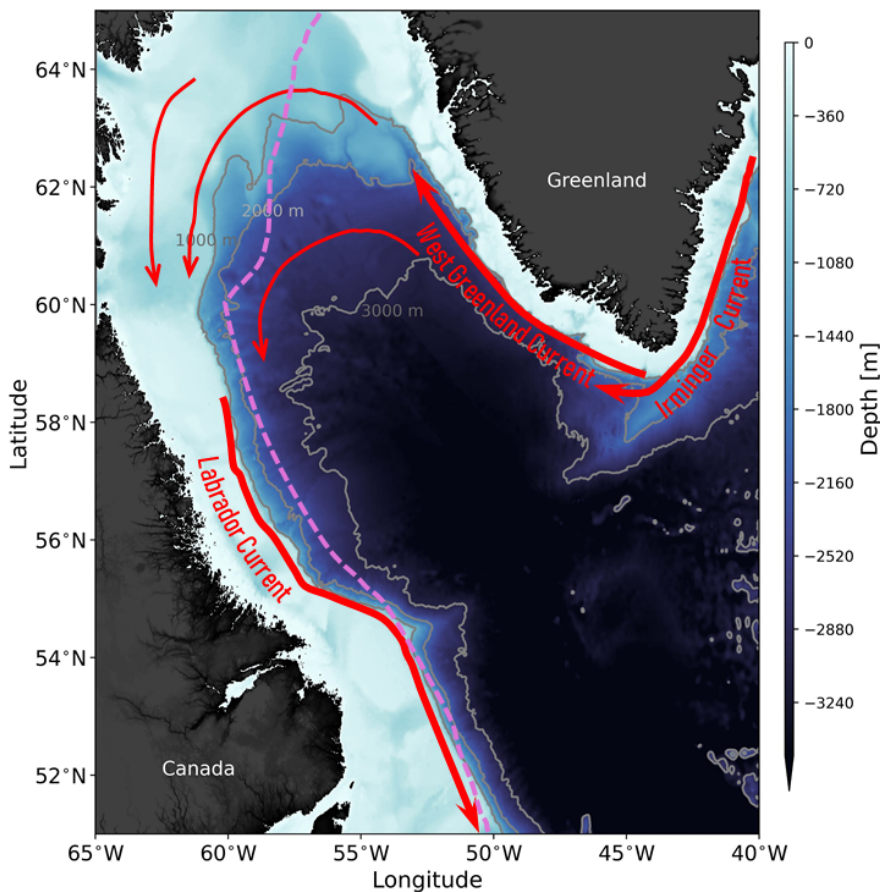


Figure 1.1: The Labrador Sea with bathymetry (Amante and Eakins, 2009) and schematic path of the Irminger, West Greenland and the Labrador Currents (adapted from Fenty and Heimbach, 2013). The magenta line represents the median sea ice edge position during March averaged over the period 1981–2010 (adapted from Scoto et al., 2022).

The deep convection process in the central part of the Labrador Sea is driven by the local surface buoyancy, which can be modulated by the complex influence of air-sea fluxes and ocean dynamics. The convection and especially restratification period in the Labrador Sea is characterized by a strong exchange of heat and freshwater between

the basin interior and boundary currents, causing a shift in interior properties towards values found in the boundary currents. This exchange is driven by lateral fluxes that transport buoyant waters originating in the Arctic and Greenland Ice Sheet. (Straneo, 2006a; Dukhovskoy et al., 2019)

Originally, based on observed warm eddies (Lilly et al., 2003), it was thought that heat was the main source influencing the restratification of the Labrador Sea. The lateral fluxes transport heat mostly from the eastern part of the Labrador Sea, i.e., from the WGC and Irminger Current to the interior. But from the Labrador Current, lateral fluxes do not transfer heat as efficiently as those from the Greenland side (Chanut et al., 2008). However, it was demonstrated that salinity is as crucial as temperature, or even more so, for the seasonal stratification of the Labrador Sea (Schmidt and Send, 2007). Low salinity anomalies have been observed to disturb and might even stop the Labrador Sea deep convection, as seen in the Great Salinity Anomaly - the large influx of freshwater from the Arctic Ocean (Dickson et al., 1988; Straneo, 2006a).

Based on observational data, it was shown that the central Labrador Sea has two separate freshwater pulses: one from April to May and one from July to September. The first pulse is of unclear origin, but the second, much stronger pulse, originates from the WGC (Schmidt and Send, 2007). This is consistent with results from numerical simulations with a $1/3^\circ$ (Myers, 2005) and $1/12^\circ$ (Pennelly et al., 2019) resolution, which showed that a significant amount of Arctic water enters the interior of the Labrador Sea through the East and West Greenland Currents. McGeehan and Maslowski (2011) suggested that April to May low salinity water intrusions might be from the Canadian shelf. In addition, recent glider observations (Clement et al., 2023) detected winter freshwater intrusions to the central part of the sea, likely originating from the Labrador Current.

Eddies play an important role in lateral fluxes between the interior and boundary currents and therefore in the restratification of the Labrador Sea (Spall, 2004; Katsman et al., 2004; Straneo, 2006b). In the Labrador Sea, two types of eddies are directly connected with offshore buoyancy fluxes. The first one is Irminger Rings - mesoscale eddies, generated by the baroclinic instability linked to the bathymetry, which are 15-30 km in radius and primarily carries heat fluxes southwestward into the basin interior (Lilly et al., 2003; Tagklis et al., 2020). The second type - eddies originate due to baroclinic and barotropic instabilities of the boundary current system (Eden

and Böning, 2002) and have sizes on the order of the Rossby deformation radius, which is around 7 km in the Labrador Sea (Spall, 2004; Chanut et al., 2008; Gelderloos et al., 2011). Although Chanut et al. (2008) showed that, in general, boundary current eddies do not propagate far from the boundary, the Labrador Current flows near the convection area and therefore eddies might affect convection (Rieck et al., 2019). Pennelly and Myers (2020) showed that increasing the model horizontal resolution to submesoscale permitting (up to $1/60^\circ$ in their case) increases the eddy kinetic energy and therefore results in greater eddy fluxes from the WGC into the interior of the Labrador Sea. Clement et al. (2023) underline the role of submesoscale eddies in the contribution to the restratification of the Labrador Sea deep convection.

Sea ice is another important factor which can affect deep convection. The decrease of Arctic sea ice has been observed in the last few decades which primarily affects the marginal ice sea dynamics, such as the Labrador Sea. McGeehan and Maslowski (2011) underline the role of sea ice position along the Labrador shelf in the modulation of freshwater flux variability and thus convection. Manucharyan and Thompson (2022), based on model results, showed that sea ice affects the submesoscale eddies' energy by frictional dissipation in ice-ocean boundary layers. The dominance of dissipation is observed during consolidated winter ice conditions, while it is significantly reduced in marginal ice zones with low concentration. Declining sea ice area and thickness leads to the removal of this dissipation mechanism. This, in turn, leads to the production of more energetic eddies, which can enhance the sea ice melt via heat exchange between the subsurface ocean and the sea ice (Manucharyan and Thompson, 2017).

In this study, we evaluate whether sea ice can suppress the freshwater fluxes, primarily by inhibiting the dynamics of mesoscale and submesoscale flows offshore the Labrador Sea coasts. We focus on the western boundary since sea ice predominantly covers the Labrador shelf (Fig. 1.1). As sea ice likely continues to shrink in a changing climate, the Labrador Current region might potentially become an important source of freshwater to the open Labrador Sea.

2

Data & Methods

Numerical model description

This study uses the latitude-longitude polar cap (LLC) numerical global ocean and sea ice simulation - the LLC4320. This is a high-resolution Massachusetts Institute of Technology General Circulation model (MITgcm) (Marshall et al., 1997) version. The model lies on the grid with $1/48^\circ$ spatial resolution (which is approximately 1km in the Labrador Sea) and 90 vertical levels with spacing increasing with depth (1m near the surface, \sim 47m near the 1000m depth and \sim 480m near the bottom). The simulation output time duration is 14 months from September 2011 to November 2012 with hourly intervals. The ocean-ice model was forced by atmospheric forcing from the 0.14° , 4-dimensional variational reanalysis product of the European Centre for Medium-Range Weather Forecasts (2011), interpolated onto the ocean grid from 6-hour time intervals, and also by the 16 most significant tidal constituents. The high-resolution ocean model output is available at the NASA ECCO Data Portal (<https://data.nas.nasa.gov/>).

Due to such a high resolution, the LLC4320 is capable of representing relatively small-scale motions such as submesoscale eddies. The model output has been widely used to study submesoscale processes in different regions at various latitudes: in the Antarctic (Siegelman et al., 2020), in mid-latitudes (Wang et al., 2022), in the Arctic (Manucharyan and Thompson, 2022).

Eddy kinetic energy and relative vorticity

To estimate eddy activity, the eddy kinetic energy (EKE) and relative vorticity are calculated. EKE shows a broad spectrum of oceanic processes with strong velocity perturbations, including mesoscale (\mathcal{O} (10-100) km) and submesoscale (\mathcal{O} (1-10) km) horizontal motions (Appen et al., 2022). It is defined as:

$$EKE = \frac{1}{2}(u'^2 + v'^2), \quad (2.1)$$

where $u'v'$ are perturbations of horizontal velocities (u, v) from their time mean state.

Relative vorticity reveals a rotating fluid, indicating eddies and associated with them submesoscale flows. The vertical component of the three-dimensional vorticity vector (ζ) describes the relative vorticity in the horizontal plane. It is given as:

$$\zeta = \frac{dv}{dx} - \frac{du}{dy}. \quad (2.2)$$

For establishing the relationship between sea ice concentration, EKE and relative vorticity in the West Greenland Current and Labrador Current region (boxes were defined in Brandt et al. (2004)), the daily averaged values are used in two approaches. In the first case, the averaged over a period with sea ice presence EKE and ζ values are binned in 5% intervals of sea ice concentration. For the second approach, bins with 1% intervals of sea ice concentration are defined for each month with sea ice. Then, the averaged EKE and ζ are calculated within the defined bins. To verify the robustness of the obtained results the bootstrap procedure (Thomson and Emery, 2014) is used as follows:

- For each percentage of sea ice concentration, all corresponding values EKE and ζ are found (EKE_{in} and ζ_{in}). These two data arrays serve as the input of the bootstrapping procedure.
- Perform sampling with replacement by randomly selecting values from input arrays (bootstrapped samples) and storing recovered EKE_{in}^* and ζ_{in}^* values.
- Repeat the previous step ten thousand times. By doing so, we store 10000 possible realizations of the recovered EKE_{in}^* and ζ_{in}^* values.
- Based on all EKE_{in}^* and ζ_{in}^* realizations, 95% confidence intervals for each percentage of sea ice concentration are computed.

Power spectral density

The horizontal velocity sections in the sea ice and sea ice-free zones are analysed in terms of spatial variability, using the following procedure:

- Signals (u and v velocities) in both zones are detrended by applying linear regression.
- Each detrended signal is decomposed (\hat{u} and \hat{v}) as a function of the wavenumber k by carrying a fast Fourier transform.
- Kinetic energy (KE) spectra for two zones are calculated as $0.5(\hat{u}^2 + \hat{v}^2)$ and time-averaged.

Wavenumber spectra are calculated on 100km sections. As a result, the KE spectral density is given as a function of wavenumber. The spatial frequency, denoted as the wavenumber, is a measure of how often a signal repeats per unit of distance. Given the unit of distance 1 km, the wavenumber is given in cycles per kilometre (cpkm). The power spectral density is in units of m^3/s^{-2} .

Potential vorticity and submesoscale instabilities

Ertel Potential Vorticity (PV) can be used to detect conditions suitable for various instabilities. When the Ertel PV (q) and Coriolis parameter (f) have opposite signs (or when q is negative in the northern hemisphere), the instabilities can develop (Hoskins, 1974):

$$q = (f\hat{k} + \nabla \times \mathbf{u}) - \nabla b < 0, \quad (2.3)$$

where $b = -g\rho / \rho_0$ is the buoyancy, with g the gravitational acceleration, ρ the density, ρ_0 - a reference density, and \mathbf{u} is the three-dimensional velocity.

However, the PV is not sufficient to distinguish between the instability types. The different instability types can arise depending on whether the vertical vorticity, stratification, or baroclinicity of the fluid is responsible for the low PV (Thomas et al., 2013). It can be shown by decomposing q in a vertical (q_{vert}) and a baroclinic (q_{bc}) component, assuming a thermal wind balanced flow:

$$q_{vert} = (f + \zeta)N^2, \quad (2.4)$$

$$q_{bc} = -\frac{1}{f} |\nabla_h b|^2, \quad (2.5)$$

where $N^2 = \frac{\partial b}{\partial z}$ is the Brunt-Vaisala frequency (or buoyancy frequency). For barotropic flows, inertial or centrifugal instability can develop when the vertical component of the relative vorticity (ζ) is anticyclonic and larger in magnitude than the f (with $N^2 > 0$). Gravitational instability occurs when the stratification is unstable (with $N^2 < 0$). Symmetric instability arises with strong lateral stratification when $|q_{bc}| > q_{vert}$ with $q_{vert} > 0$.

Thomas et al. (2013) showed that the dominant type of instability can be identified by the finite balanced Richardson angle (ϕ_{Ri_b}):

$$\phi_{Ri_b} = \tan^{-1}\left(-\frac{|\nabla_h b|^2}{f^2 N^2}\right), \quad (2.6)$$

instabilities can be observed when $\phi_{Ri_b} <$ the critical angle (ϕ_c). With the vertical component of the absolute vorticity of the geostrophic flow ($\zeta_g = f + \nabla \times \mathbf{u}_g \cdot \hat{k}$), the ϕ_c can be defined as:

$$\phi_c = \tan^{-1}\left(-\frac{\zeta_g}{f}\right). \quad (2.7)$$

The scheme in Fig. 2.1 shows how these two angles (ϕ_{Ri_b} and ϕ_c) can be used to distinguish between the various instabilities. As it was mentioned above, gravitational instability (GI) occurs for $N^2 < 0$ and weak lateral stratification ($\nabla_h b \sim 0$), which is equivalent to $-180^\circ < \phi_{Ri_b} < -135^\circ$. With stronger baroclinicity and still unstable stratification, the mixed regime between GI and symmetric instability (SI) (SI/GI) arises at $-135^\circ < \phi_{Ri_b} < -90^\circ$. SI develops for $-90^\circ < \phi_{Ri_b} < \phi_c$ when stratification is weak, but stable. For anticyclonic vorticity $\phi_c > -45^\circ$ ($\phi_c < -45^\circ$ for cyclonic) a hybrid SI/inertial instability (SI/II) occurs for $-45^\circ < \phi_{Ri_b} < \phi_c$. Outside these unstable regimes (for $\phi_c < \phi_{Ri_b} < 0^\circ$), the flow is stable.

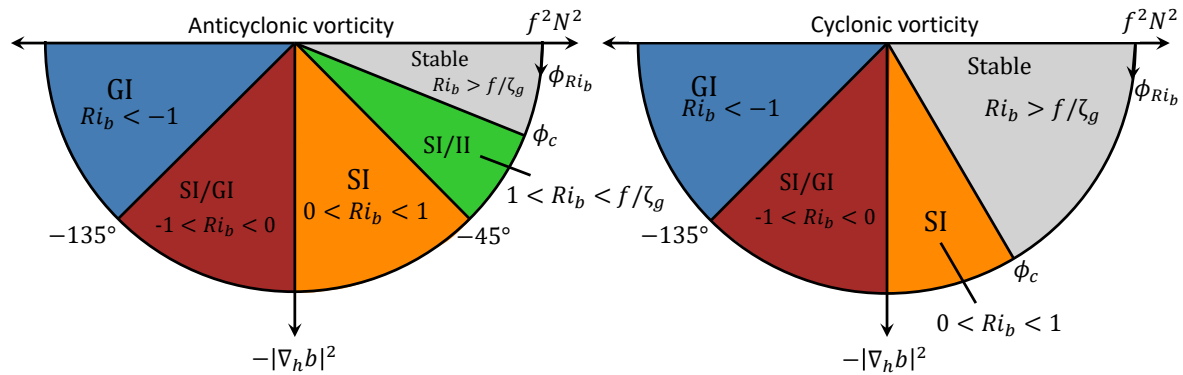


Figure 2.1: Schematic illustrating the relation between the angle ϕ_{Ri_b} (2.6) to the gravitational (GI), symmetric (SI) and inertial (II) instabilities that arise when $f q < 0$ and the vorticity is anticyclonic (left) and cyclonic (right). The dependence of ϕ_{Ri_b} on the baroclinicity and stratification is also indicated. Adapted from Thomas et al. (2013).

Freshwater anomalies

To estimate the potential impact of sea ice on freshwater transport by eddies from the boundary current the freshwater content is vertically (z) integrated:

$$FW_z = \int_0^z FW' dz, \quad (2.8)$$

where FW denotes freshwater content calculated from salinity (S) and a reference salinity (S_{ref}) as $FW = (S_{ref} - S)/S$. S_{ref} of 34.8 is used, the number is based on the literature focused on the Labrador Sea (Aagaard and Carmack, 1989; Pennelly et al., 2019). The prime in Eq. 2.8 denotes submesoscale anomaly obtained relative to \sim 25km moving average.

To distinguish the difference between freshwater content under sea ice and in a sea ice-free zone the mean FW in both areas are taken. The Student's t-test is used to determine whether there is a significant difference between the means of the two zones with 95% significance level (Thomson and Emery, 2014):

$$T = \frac{\overline{FW}_{ice} - \overline{FW}_{sea}}{\sqrt{\frac{\sigma_{ice}^2}{n_{ice}} - \frac{\sigma_{sea}^2}{n_{sea}}}}, \quad (2.9)$$

where σ denotes the standard deviation and n - length of an array.

All the calculation is done using Python programming language. For the LLC4320 output data analysis, including the Ertel PV calculation, the OceanSpy package (Almansi and Gelderloos, 2019) is used.

3

Results

Sea ice, eddy kinetic energy and relative vorticity

To establish the relationship between sea ice and mesoscale formations, we first look at sea ice concentration, surface eddy kinetic energy (EKE) and relative vorticity distributions at different time steps with varying sea ice conditions (Fig. 3.1). In sea ice-free areas, the EKE and relative vorticity distributions occur on various spatial scales, including small-scale features, and magnitudes reach high values ($EKE > 1000 \text{ cm}^2/\text{s}^2$, relative vorticity $> | 4 * 10^{-5} | \text{ s}^{-1}$). In contrast, under sea ice, these parameters, in general, are smoothed and mesoscale processes become much less pronounced. The magnitude of the values is lower in sea ice zones compared to sea areas which are free from ice. Under sea ice, the relative vorticity values are less than $| 1.5 * 10^{-5} | \text{ s}^{-1}$ and EKE values are less than $400 \text{ cm}^2/\text{s}^2$. However, there are some exceptions. The pronounced structure of eddies and filaments with high EKE and relative vorticity values still can be found even in regions with high sea ice concentration. In the shelf break area, along the 1000m isobath, high EKE values (up to $1000 \text{ cm}^2/\text{s}^2$) are observed in the southwest part of the Labrador Sea during January (second row in Fig. 3.1). Large mesoscale eddies and associated with them high relative vorticity ($\sim | 4 * 10^{-5} | \text{ s}^{-1}$) and EKE (up to $1000 \text{ cm}^2/\text{s}^2$) values are found in the northeast part of the sea around Greenland in January and March (second and third row in Fig. 3.1). These areas, primarily, are boundary current regions - Labrador Current (LC) and West Greenland Current (WGC) (red dashed boxes in Fig. 3.1). High eddy activity in these regions, especially in the WGC, is supported by barotropic and baroclinic instabilities (Eden and Böning, 2002).

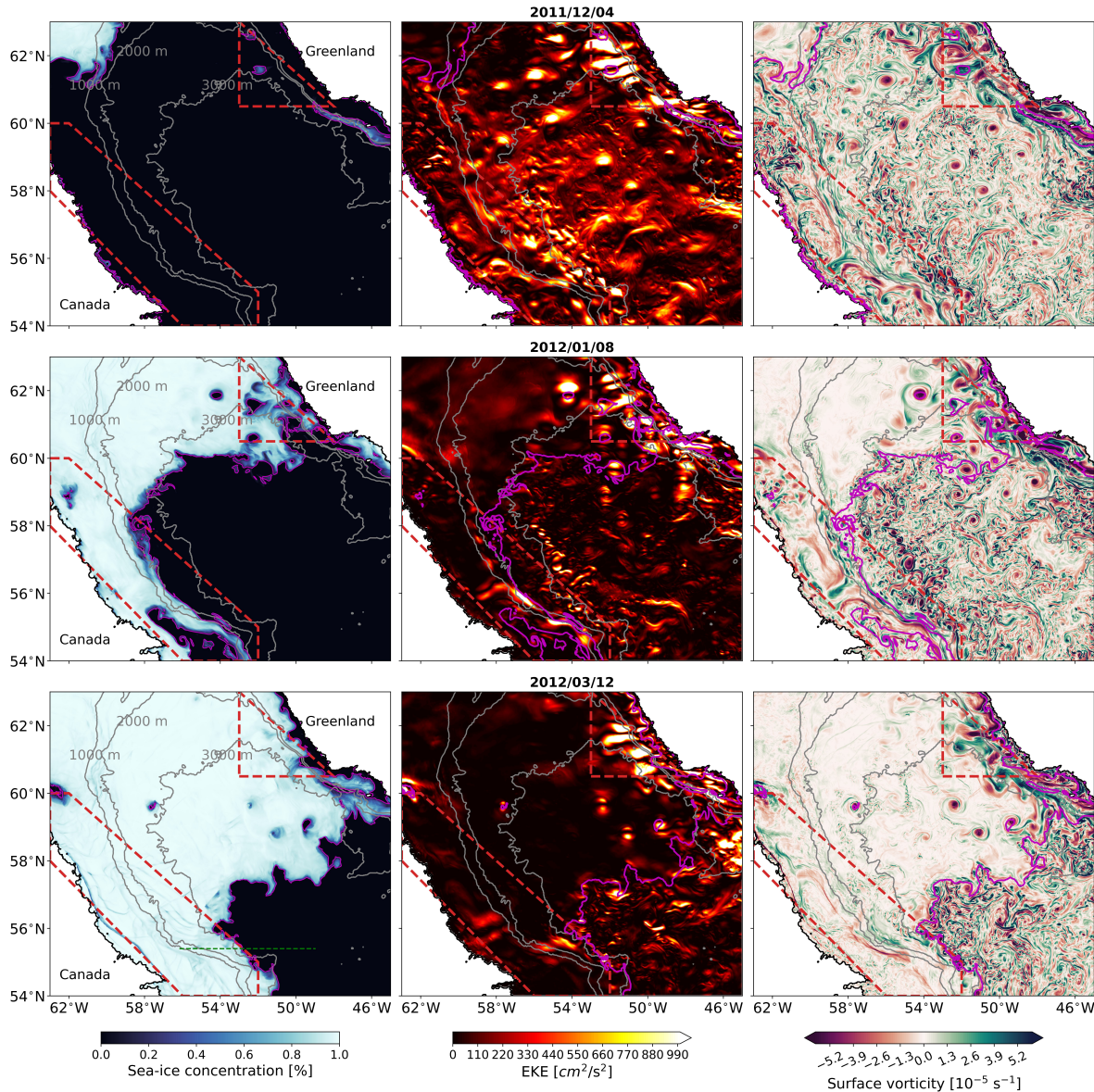


Figure 3.1: Snapshots of 2011-12-04 (1 row), 2012-01-08 (2 row) and 2012-03-12 (3 row) of Sea Ice Concentration (1 column), EKE (2 column) and Relative Vorticity (3 column) distribution. The magenta line represents 10% of sea ice concentration. Grey contours represent 1000m, 2000m and 3000m isobaths. Red dashed boxes denote the LC and WGC regions defined in Brandt et al. (2004).

The green line in 2012-03-12 denotes a $\sim 400\text{km}$ transect used in the Fig. 4.8

Based on previous works (Eden and Böning, 2002; Brandt et al., 2004) the maximum eddy kinetic energy is observed during winter, in February for the LC region, when the boundary currents are strongest. However, this is not the case with the LLC4320 model. While we still can see the high EKE values in the WGC region under the sea ice, the values in the LC region are significantly lower during high sea ice concentration times (compare the first and third row of Fig. 3.1). This discrepancy with previous works could potentially be due to the overestimated representation of sea ice in the LLC4320 model. The March sea ice extent in the LLC4320 (third row in Fig. 3.1) is far

beyond the climatological sea ice edge (Fig. 1.1).

The dissimilarity can also be seen in the comparison of the monthly mean, spatially averaged EKE values in two regions (WGC and LC) between LLC4320 data and satellite observations (Brandt et al., 2004), which is presented in Figure 3.2. The maximum EKE in the WGC region according to satellite data is around $800 \text{ cm}^2/\text{s}^2$ and observed in January. The LLC4320 EKE in January is lower than $400 \text{ cm}^2/\text{s}^2$. Moreover, there is no pronounced maximum in the annual cycle in the model results, the highest values are observed in February, May and November and they are around $500 \text{ cm}^2/\text{s}^2$. In the LC region, the maximum of satellite EKE is observed in March and it is slightly larger than $500 \text{ cm}^2/\text{s}^2$, while modelled March EKE values are lower than $100 \text{ cm}^2/\text{s}^2$ and it is a minimum in its annual cycle. The largest values of modelled EKE in the LC region are observed during October and December and are about $200 \text{ cm}^2/\text{s}^2$. The smallest difference between observation and model values is during summer and at the beginning of autumn when EKE is supposed to have the lowest values on its seasonal cycle. However, the difference increases from December to May, especially in the LC region. These are months of high sea ice extent and when EKE is expected to reach maximum values in its seasonal cycle. This large difference between satellite observation and the LLC4320 model is due to very low values in the latter, which is potentially caused by unrealistically broad sea ice cover. Overall, the discrepancy between the two sources of data and the unrealistic high sea ice extent in the model during months of the largest difference is in agreement with the hypothesis of submesoscale and mesoscale suppression by sea ice.

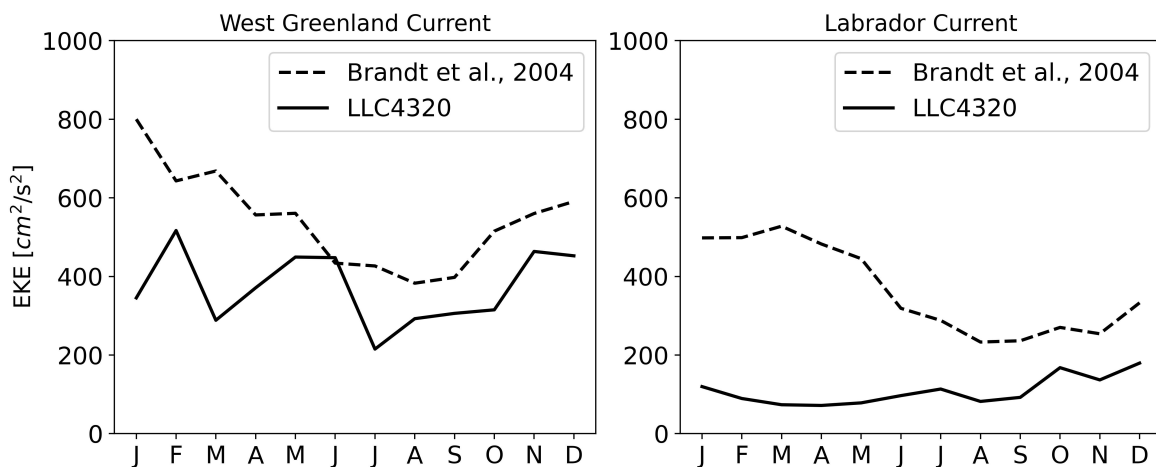


Figure 3.2: Monthly mean values of EKE in the WGC and LC regions from satellite observations (dashed line – Brandt et al. (2004)) and model output (solid line – LLC4320).

To define the general patterns of the relationship between EKE, relative vorticity and sea ice and also reduce the impact of unrealistic sea ice distribution in the model, such as polynyas in the open sea and high sea ice extent (Fig. 3.1), time-averaged datasets are analyzed (Fig 3.3). The period of averaging is the time range with sea ice presence in the LLC4320 – from the 1st of December to the 15th of May. The values on the shelves (up to 900 m isobath) are masked to remove the influence of the dynamic processes on the shelf.

The WGC region has high eddy kinetic energy (Fig. 3.3b) and a high magnitude of relative vorticity (Fig. 3.3c). At the same time, most of the region is covered with sea ice with a concentration of less than 50% (Fig. 3.3a). The southeast part of the region along the shelf break, which corresponds to the path of the West Greenland Current, has the largest in the region EKE ($>700 \text{ cm}^2/\text{s}^2$) and relative vorticity ($>3.5 * 10^{-5}\text{s}^{-1}$) values with weakly consolidated sea ice ($\sim 20\%$ sea ice concentration). Even in the western part of the region with sea ice concentration $> 50\%$, EKE and relative vorticity values are still large, up to $700 \text{ cm}^2/\text{s}^2$ and $3 * 10^{-5}\text{s}^{-1}$ respectively. The lowest values of EKE ($<100 \text{ cm}^2/\text{s}^2$) and relative vorticity ($< 1.5 * 10^{-5}\text{s}^{-1}$) are observed in the southwest part of the area. Most likely, these values are related to the large distance from the source of eddy generation (West Greenland Current) and not to the presence of sea ice with concentration $>50\%$. As it is also known from the literature (Lilly et al., 2003; Tagklis et al., 2020), the WGC region is one of the main sources of warm-core eddies which may potentially reduce the sea ice extent. In the end, this cannot explicitly point out the dependency of (sub)mesoscale formations on sea ice but rather the opposite - the presence of warm and energetic eddies can modulate (melt) sea ice in this region.

The LC region is mostly covered by sea ice with high concentration, almost half of the region is covered with sea ice concentration larger than 70%. Sea ice concentration $<50\%$ is observed only in a small section in the southwest part of the region along the 3000m isobath. EKE and relative vorticity are generally weaker than in the WGC area and high values are only observed with the low sea ice concentration. The maximum of EKE is around $250 \text{ cm}^2/\text{s}^2$ and relative vorticity reaches the magnitude of $3.5 * 10^{-5}\text{s}^{-1}$, which is comparable with values in the WGC region. At the same time, the area covered by high relative vorticity values in the LC region is noticeably smaller than in the WGC region. The magnitude of both, EKE and relative vorticity, parameters decreases toward the shallow water and is inversely proportional to the

increase in sea ice concentration. In this region, eddies are primarily generated due to baroclinic instabilities (Eden and Böning, 2002) of the Labrador Current, which transports cold and fresh waters. To sum it up, the high sea ice concentration, which has the potential to suppress small-scale processes, and the lack of warm eddies in the LC region indicate a relationship where sea ice influences ocean small-scale dynamics. While in the WGC region, the presence of warm (sub)mesoscale eddies might lead to the sea ice melt.

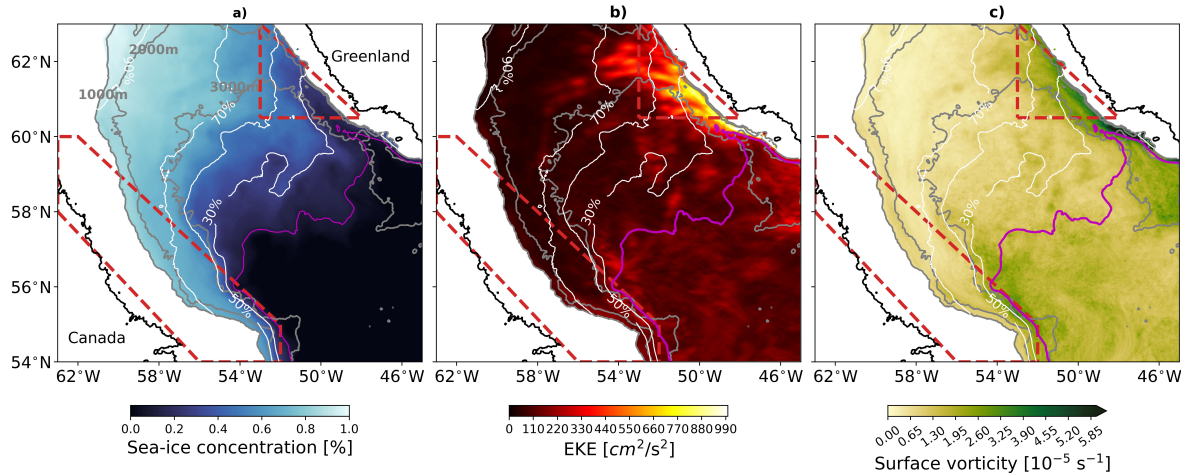


Figure 3.3: Time averaged (from the 1st of December to the 15th of May) Sea Ice Concentration (a), EKE (b) and Relative Vorticity (absolute values) (c) distributions. White contours represent 30%, 50%, 70% and 90% of sea ice concentration. The magenta line, grey contours and red dashed boxes same as in Fig. 3.1.

For a detailed analysis of sea ice connections with mesoscale formations, the time-averaged EKE and relative vorticity (in absolute values), which are presented in Fig. 3.3, are binned according to 5% intervals of time-averaged sea ice concentration (Fig. 3.4).

As discussed above, the causality in EKE and sea ice relationship is not clear in the WGC region, there is almost a linear inverse relationship between EKE and sea ice concentration. High EKE values up to almost $1000 \text{ cm}^2/\text{s}^2$ in the region occur with the presence of low sea ice concentration (around 20%) and with decreasing of EKE magnitude there is a constant increase of concentration. In the LC region, where (sub)mesoscale eddies are supposed to be modulated through sea ice, the EKE values are generally lower in comparison with the WGC region ($< 350 \text{ cm}^2/\text{s}^2$) and eddy kinetic energy seems to not respond to changes in sea ice concentrations. However, high sea ice concentration ($> 60\%$) in that region reduces EKE values down to 0 (first row in Fig. 3.4). Therefore, there is potentially a critical value of sea ice concentration

after which sea ice significantly decreases EKE.

The sea ice connection with relative vorticity has a similar behaviour as the relationship between EKE and sea ice, but with some noticeable differences (second row in Fig. 3.4). In both regions the magnitude of relative vorticity reaches the same numbers - up to $4.5 \times 10^{-5} s^{-1}$. However, most of the relative vorticity in the LC region, as well as EKE, is concentrated in the area of low values ($< 1.5 \times 10^{-5} s^{-1}$) and the sea ice concentration boundaries between 60% and 80%. At the same time, in the WGC region values are distributed more evenly from $4 \times 10^{-5} s^{-1}$ to $0.5 \times 10^{-5} s^{-1}$ and occur within the larger changes in sea ice concentration from 20% to 70%. In addition, in the WGC region, the pattern of the connection between relative vorticity and sea ice is similar to the sea ice connection with EKE - a strong inversely proportional relationship is observed. In the LC region, on the other hand, the magnitude decrease seems to be across the whole spectrum of sea ice concentration, while with EKE it is less visible.

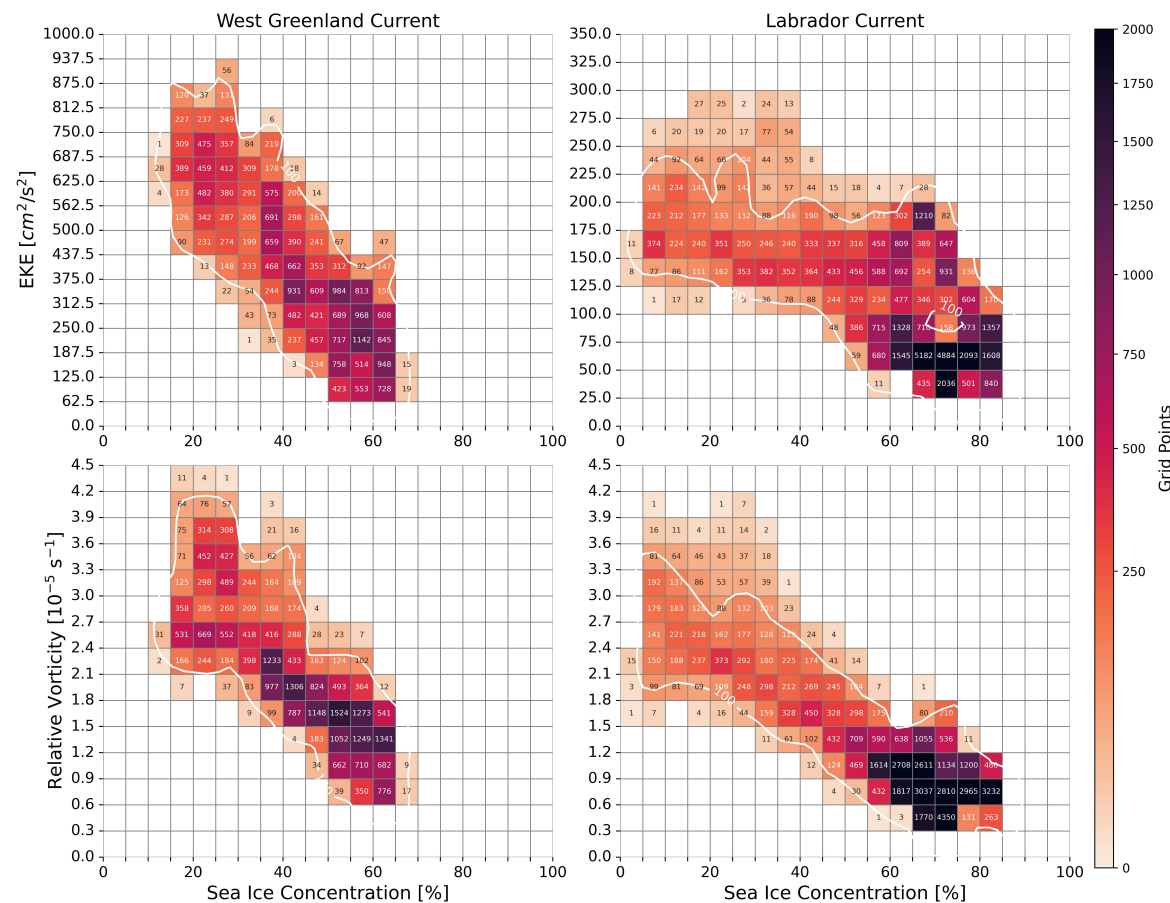


Figure 3.4: Heatmaps of time-averaged (from the 1st of December to the 15th of May) EKE vs Sea Ice Concentration (**First row**) and Relative Vorticity vs Sea Ice Concentration (**Second row**), colors represent numbers of grid points in a bin. Two regions are presented: WGC (left) and LC (right).

Although the use of time-averaged values can show a general relationship between EKE/relative vorticity and sea ice, the time averaging over such a specific period may result in smoothing out the daily variations and short-term dynamics. In addition, spatial variability in sea ice concentration, EKE and relative vorticity may not be fully captured in a time-averaging approach. As a result, it smooths any extremes such as high (up to 100%) and low (down to 0%) sea ice concentration and associated EKE and relative vorticity values, and therefore, this method cannot give a full picture of the relationship between sea ice and (sub)mesoscale dynamics. For that reason, another way of data analysis is presented. In the second approach, we average EKE and relative vorticity values for each % of sea ice concentration within a single month. The results with 95% confidence intervals, calculated using the bootstrap procedure, are presented for each month with the presence of sea ice (from December to April) in Fig. 3.5.

The strong connection between EKE and sea ice in the WGC region is much less visible now (compare the first rows in Fig. 3.5 and Fig. 3.4 for the WGC region). However, there is still an increase in sea ice concentration with a decay of EKE in the months of highest sea ice extent - February and March. As well as in April, when sea ice does not extend far. The peak of EKE at around 20% of sea ice concentration during April is related to steady mesoscale eddies in the region (not shown in a figure). In the LC region, the relationship behaviour, in general, is in agreement with the results discussed above. As sea ice increases, EKE stays relatively constant for most ice-covered months and only begins to decrease when sea ice is highly consolidated (from $\sim 80\%$ concentration). Moreover, even in the WGC region, this break in scaling is noticeable in February - the month with the largest sea ice extent and when EKE has the maximum values on its seasonal cycle. Based on the identified break in scaling, it can be concluded that there is a weak relationship between EKE and sea ice at low concentrations, but at very high ice concentrations (greater than 80%), at least in the Labrador Current, eddies may be suppressed by sea ice, irrespective of the month considered (December through May).

The connection between sea ice and relative vorticity appears to be more robust compared to the relationship between sea ice and EKE (second row in Fig. 3.5). Inversely proportional sea ice concentration connection with relative vorticity is observed in both regions based on calculations for each ice-covered month, confirming the patterns observed in the time-averaged data (second row in Fig. 3.4). The stronger

sea ice connection with relative vorticity (in comparison with EKE) suggests that relative vorticity, as a measure of the rotation of fluid may have a more direct and immediate response to sea ice changes, while eddy kinetic energy, as a representation of the energy associated with oceanic eddies, decreases only with high sea ice concentration. However, the scale break at 80% of sea ice concentration is also observed with relative vorticity in both regions almost every month with sea ice.

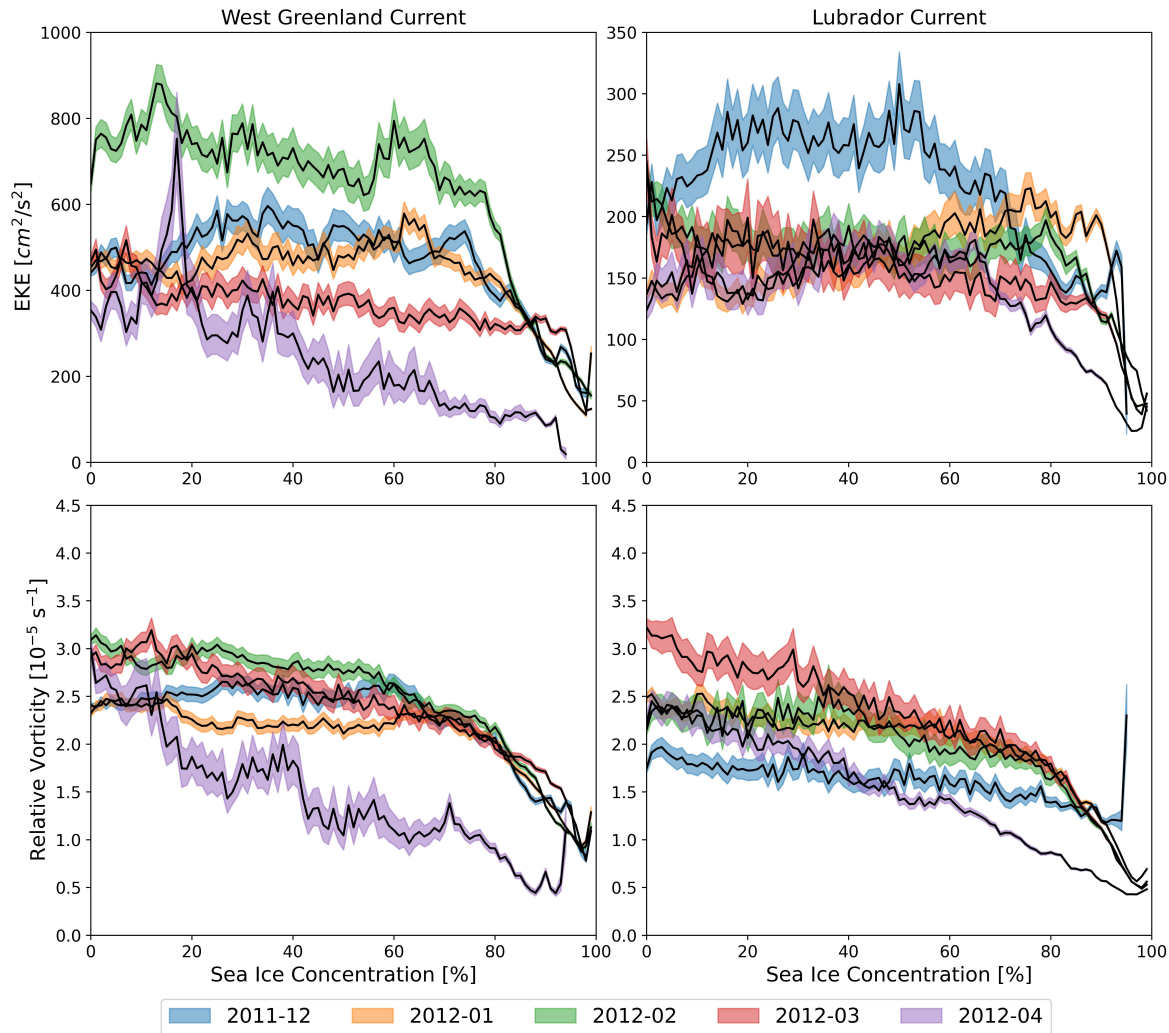


Figure 3.5: Averaged EKE (First row) and Relative Vorticity (Second row) for each % of Sea Ice Concentration, shadows represent the 95% confidence intervals. Two regions are presented: WGC (left) and LC (right).

While the representation of Labrador sea ice in the LLC4320 may be overestimated, the model remains a powerful tool that enables the analysis of the relationship between sea ice and (sub)mesoscale formations. This section presents results from two distinct approaches studying the connections of surface EKE and relative vorticity with sea ice concentration in regions characterized by different cause-and-effect dynamics. The behaviour of sea ice connection with EKE and relative vorticity, as

two parameters that represent, among others, (sub)mesoscale dynamics, but from different perspectives, has both similarities and differences. The sea ice link with relative vorticity appears more pronounced than with EKE. At the same time, the scale break at 80% of sea ice concentration is observed in both parameters.

Submesoscale dynamics under sea ice and in sea ice free zone

The sea ice connection with surface EKE and relative vorticity discussed above suggest that high sea ice concentration suppresses eddy intensity, especially in the Labrador Current region. To further investigate the sea ice effects and compare the ocean dynamical processes under the sea ice and in the ice-free zone, we look at the sub-domain across the sea ice edge in the Labrador Current region, with 100 and 400 km sides, during the time of the largest sea ice extent (Fig. 3.6).

First of all, sea ice is blocking the ocean heat exchange with the atmosphere. The ocean-atmosphere heat flux is around zero in the sea ice zone. At the same time, in the sea-ice-free area, the heat flux is negative (the axis is directed to the ocean) and decreases away from the sea ice edge (Fig. 3.6a). The heat flux directed from the ocean to the atmosphere leads to surface cooling off, which in turn leads to a deeper mixed layer (Fig. 3.6d and black contours in Fig. 3.6a). In this study, the mixed layer depth is defined by a density threshold of $\sigma_p = 0.01 \text{ kg m}^{-3}$ relative to a shallow reference at 10 m (Thomas et al., 2015).

The previous section analysed the surface relative vorticity and its connection with sea ice. Here, we take a look at the relative vorticity dynamics at the 100 m depth (Fig. 3.6b). Although the relative vorticity under the ice, as in the sea ice-free zone, reaches high values ($> 5.5 * 10^{-5} \text{ s}^{-1}$), its spatial structure appears smoother, while in the open sea, the relative vorticity has filament and eddy patterns. On the peripheries of these eddies and filaments, submesoscale instabilities can grow (Taylor and Thompson, 2023). These submesoscale instabilities might induce strong vertical velocities of $O(10^{-3}) \text{ m s}^{-1}$ (Thomas et al., 2008). Therefore, the regions with high vertical velocities might indicate the areas with high submesoscale activity. The relatively high vertical velocity values (up to $2 * 10^{-3} \text{ m s}^{-1}$) at 100 m depth (Fig. 3.6c), which are probably associated with submesoscale instabilities, are found in the open sea areas with deep mixed layer depth (Fig. 3.6d). Although there are vertical velocities with large magnitudes ($> 2 * 10^{-3} \text{ m s}^{-1}$) under the sea ice as well (in the down-left corner of Fig. 3.6c), the spatial scales of these velocities are bigger than in the sea ice-free zone, and therefore these values cannot be unequivocally associated

with a submesoscale origin. To sum it up, the active interaction with the atmosphere, facilitated by open sea areas and the resulting ocean cooling, deepens the mixed layer, favouring the development of submesoscale formations. This is evidenced by the observed high vertical velocities and filamentary/eddy structures, even at the 100 m depth, particularly in regions with deep mixed layer depth.

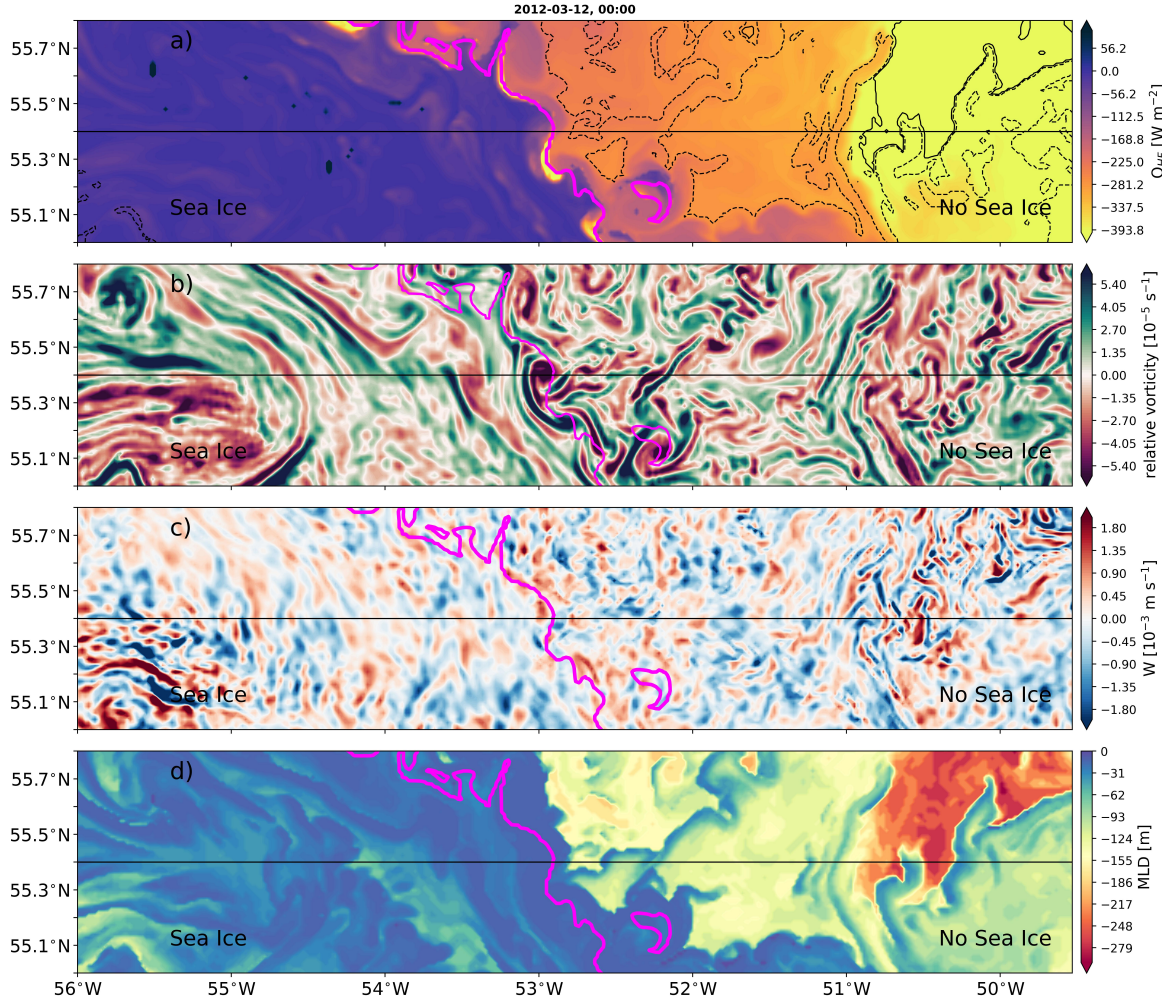


Figure 3.6: Atmosphere-ocean heat flux (a), relative vorticity (b) and vertical velocity (c) at the 100m depth, and mixed layer depth (d). The magenta line represents 10% of sea ice concentration, which separates sea ice and no sea ice zones. The dashed and solid contours in (a) represent 100m and 200m mixed layer depths respectively.

Figure 3.7 illustrates the time-averaged kinetic energy (KE) spectral density ($m^3 s^{-2}$) as a function of the wavenumber k (spatial frequency) given in cycles per kilometre (km^{-1}) for near-surface (6m depth) and 100m depth. The average period is from March 12 to March 16 with a 6-hour interval. The spectral analysis covers both sea ice and sea ice-free areas (two sections along the black solid line in Fig. 3.6), aiming to explore the differences in spatial variability of ocean dynamics between those two zones.

Kinetic energy is higher at the larger spatial (mesoscale) scales and decreases at smaller (submesoscale) scales. At the near-surface layer, KE decrease is starting to slow at spatial scales around 50km and then accelerating again at $\sim 15\text{km}$ under the sea ice, while in the sea ice-free zone, the decreasing accelerates at smaller scales ($\sim 12\text{km}$). This, in turn, leads to spectra separation at small spatial scales with more KE in the open sea areas. At the 100m depth, a slower KE decrease is observed between 50km and 30km in the open sea area, while in the sea ice zone, it does not seem to slow down at any spatial frequency. This leads to spectra separation even at the larger spatial scales (around 30 km) in comparison with the near-surface layer. As expected from the snapshot on March 12 at 00:00 of relative vorticity (Fig. 3.6b), the KE spectral density in the two zones shows the presence of more energetic submesoscale features in the sea ice-free zone compared to the dynamic under the sea ice. Moreover, this pattern is observed both in the near-surface layer and at a depth of 100m.

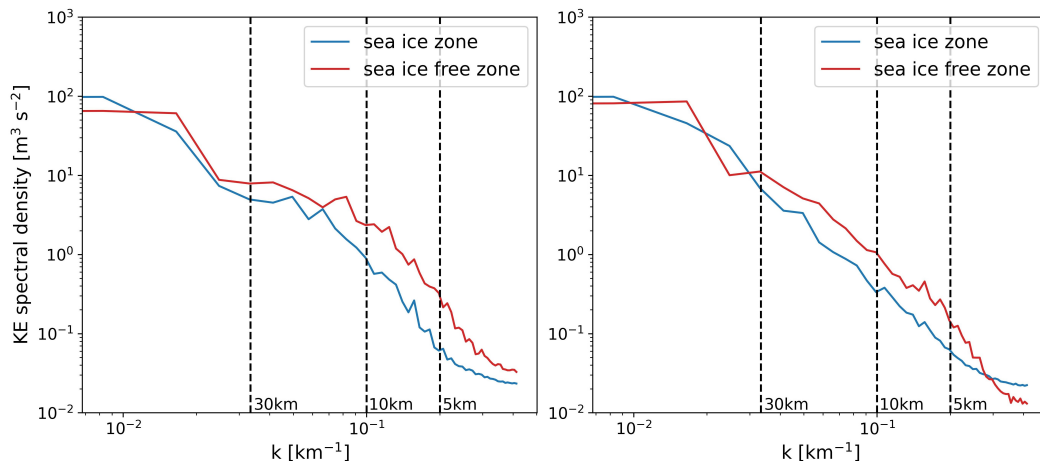


Figure 3.7: Spectral densities of near-surface (left) and depth (right) kinetic energy were diagnosed at 6 m and 100 m depth respectively for sea ice (blue colors) and sea ice free (red colors) zones.

However, it is important to mention that these results are not proven by confidence intervals. Including confidence intervals in the analysis of the KE spectral density would provide a statistical measure of uncertainty, allowing for enhancing the reliability of the conclusions. Nevertheless, in noticeable contrast to the under-ice ocean dynamics is the increase in submesoscale activity in the sea ice-free zone, both in the near-surface layer and at a depth of 100 m.

To investigate types of submesoscale instabilities, the finite balanced Richardson angle ϕ_{Ri_b} is presented on the transect through a sea ice edge (black solid line in Fig. 3.6 and dashed green line in Fig. 3.1) along with the vertical structure of potential density, Ertel Potential vorticity and lateral buoyancy gradient - Fig. 3.8.

While negative potential vorticity can show the presence of submesoscale instabilities, ϕ_{Ri_b} allows to determine the conditions causing a certain type of instability. For instance, between 250km and 300km, the lateral buoyancy gradients b_x were small and negative potential vorticity values in that region were primarily due to gravitational instabilities (blue colors in Fig. 3.8a). The large b_x , as observed around 225km and 340km, within the mixed layer (the mixed layer depth is denoted as the orange line in Fig. 3.8) correspond to slanted isopycnals and weak but stable stratification (Fig. 3.8b). The strong lateral buoyancy gradients and small but positive N^2 are responsible for keeping the potential vorticity below 0. Therefore, these conditions, as discussed in the Data & Methods chapter, are suitable for the development of symmetric instabilities, which are denoted as orange spots in Fig. 3.8a.

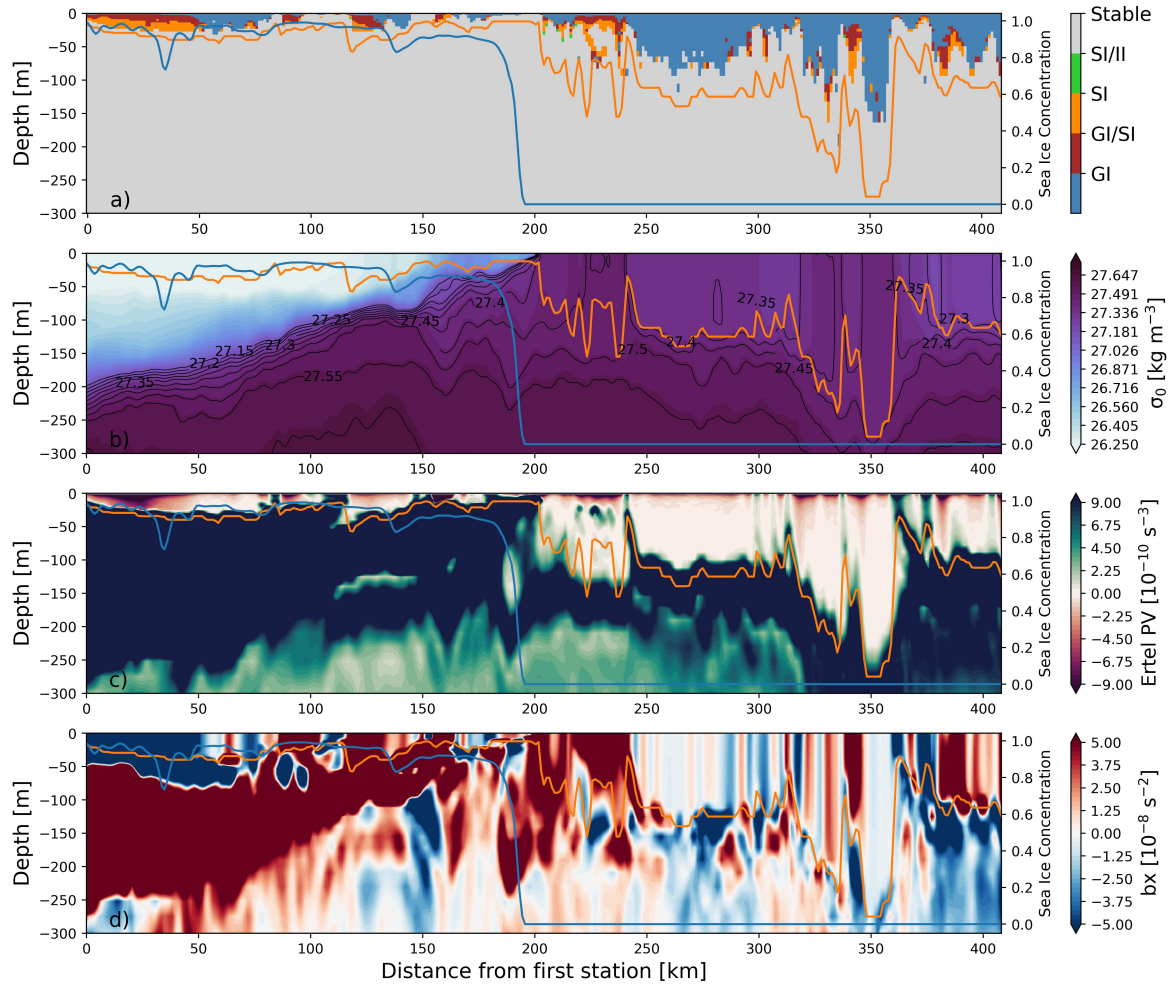


Figure 3.8: (a) Overturning instabilities arising for negative potential vorticity: gravitational instabilities (GI in blue), symmetric instabilities (SI in orange), mixed regime gravitational/symmetric instabilities (GI/SI in red), mixed regime symmetric/inertial instabilities (SI/II in green) and stable conditions (grey). (b) Potential density. (c) Ertel Potential vorticity. (d) Lateral buoyancy gradient b_x . The mixed layer depth is indicated in orange and the sea ice concentration is added in blue in (a)–(d).

Submesoscale instabilities may occur not only at the sea ice-free zone, where its presence is supported by relative vorticity patterns (Fig. 3.6b) but also in the region with high sea ice concentration, even 150km away from the sea ice edge. The structure and extent of instabilities within the two zones are different though. In the sea ice zone, SI are spreading in a blob-shaped manner, which can be seen between 0 and 50 km in Fig. 3.8a. In the ice-free zone, however, SI are located mostly pointwise between GI, which is visible, for instance, around ~ 340 km and ~ 380 km in Fig. 3.8a. Under the sea ice, there are large b_x , however the strong stratification beyond the mixed layer keeps the conditions stable and prevents the generation of instabilities. In the ice-free zone, SI can occur below GI, which is in agreement with Taylor and Ferrari (2010), whereas under the sea ice, the SI occupy most of the mixed layer. Moreover, since sea ice blocks the exchange with the atmosphere, the mixed layer depth is shallower in the sea ice zone. This leads to a shrink of conditions (weak or unstable stratification) for submesoscale instability development. Therefore, the deeper penetration of submesoscale instabilities in the sea ice-free zone (~ 150 m), compared with the instability distribution under the sea ice (~ 25 m), is a direct outcome of the free exchange with the atmosphere.

Potential impact on the lateral freshwater fluxes

The kinetic energy spectrum shows decreased submesoscale dynamics under the sea ice. At the same time, the comparison of small-scale dynamics in two areas with different sea ice conditions indicates the presence of submesoscale instabilities under sea ice but with shallower penetration than in the ice-free zone. Given that eddies originating in the Labrador Current region are capable of capturing and transporting significant amounts of freshwater (Schmidt and Send, 2007; McGeehan and Maslowski, 2011; Pennelly et al., 2019), we assess whether suppression of eddy intensity and restriction of the submesoscale instability depth penetration by sea ice leads to a decrease in freshwater fluxes from the boundary current to the Labrador Sea interior.

To investigate the potential impact on freshwater fluxes, we look at the sea surface salinity and surface relative vorticity during the time of low (on December 29, Fig. 3.9a-b) and high sea ice extent (on March 12, Fig. 3.9c-d). Around the Labrador Current, during the time without sea ice, the salinity and relative vorticity are higher than with sea ice presence. In addition, surface salinity and relative vorticity on December 29 have a similar pattern and highlight the stronger submesoscale activity

in the region. On March 12, the Labrador current waters (west of 53°W) are fresher and the waters east of 53°W are saltier than on December 29. This might indicate the weaker lateral exchange of boundary current waters with the interior. The presence of large amounts of freshwater under the sea ice is also confirmed by a vertically integrated freshwater anomaly (Fig. 3.9e). Anomaly here refers to the deviation from the ~25 km moving average to highlight submesoscale anomalies. The Student's t-test shows that there is a significant statistical difference between means of freshwater anomalies in ice-free (0.02m) and sea-ice (0.45m) zones.

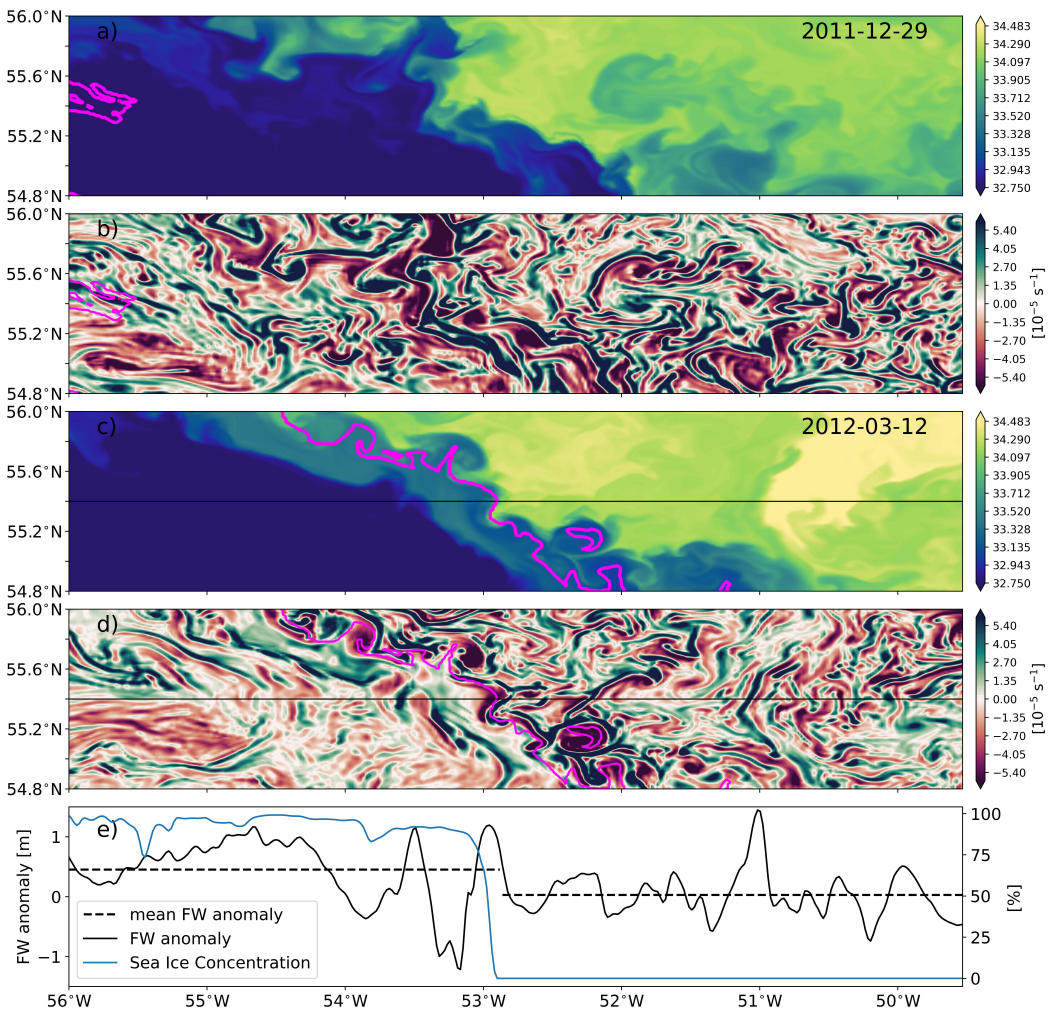


Figure 3.9: Surface salinity (a, c) and relative vorticity (b, d) for 2011-12-29 (a-b) and 2012-03-12 (c-d). e - Vertically integrated freshwater (FW) anomaly (black solid line), sea ice concentration (blue line) and mean FW anomalies for sea ice and sea ice-free zones (dashed black lines) from a transect (black line in c-d) on 2012-03-12. The magenta line same as in Fig.3.6.

The observed distinction between the two zones with different sea ice conditions, as evident in the sea surface salinity, relative vorticity and freshwater content (Fig. 3.9c-e), indicates the potential presence of a boundary influencing the lateral exchange between the Labrador Current and the deep convection area.

4

Conclusion

This study has examined the influence of sea ice changes on (sub)mesoscale flows offshore the Labrador Sea coasts, particularly focusing on the Labrador Current region using high-resolution numerical simulation.

Highly consolidated sea ice (with a concentration greater than 80%) greatly reduces the intensity of eddies, which is evident from the relationship of sea ice concentration with EKE and relative vorticity. Moreover, the relative vorticity exhibits a more direct and immediate reaction to variations in sea ice compared to eddy kinetic energy. The suppression of submesoscale eddy intensity is also confirmed by power spectral density analysis of kinetic energy which has shown the presence of more energetic submesoscale movements in the sea ice-free zone in comparison with the dynamic under the sea ice.

Although there is a clear reduction in mesoscale and submesoscale eddy strength under the ice, high vertical velocity values ($>2 * 10^{-3} \text{ m s}^{-1}$) could potentially indicate the presence of submesoscale features even in areas of strongly concentrated sea ice. Indeed, the negative potential vorticity and identification of specific types of instabilities indicate the presence of submesoscale instabilities not only in sea ice-free zones but also under the sea ice, even more than 150km away from the sea ice edge. This is consistent with Manucharyan and Thompson (2017) results, which show that ocean submesoscale instabilities can extend under relatively packed sea ice. However, strong sea ice conditions block heat loss to the atmosphere, thereby reducing the mixed layer depth. This, in turn, limits favourable conditions, such as weak or unstable stratification, for the development of submesoscale instabilities. Despite

the presence of large buoyancy gradients below the mixed layer under the sea ice, strong stratification keeps the water column stable and prevents the generation of any instabilities. As a result, submesoscale instabilities in open sea areas penetrate to a deeper level compared to the regions covered by sea ice.

Sea surface salinity patterns and high eddy activity during periods of low sea ice extent indicate that low-salinity water intrusions from the Labrador Current might have eddy/filamentary structure. However, as sea ice extent increases, a boundary separating the relatively fresh waters of the boundary current and the central Labrador Sea with high-salinity water develops, potentially leading to a decrease in offshore lateral exchange.

Altogether, the observed reduction in Arctic sea ice, including in the Labrador Sea, in the context of a changing climate may lead to increased freshwater flux from the western coast of the Labrador Sea into the deep convection region via (sub)mesoscale formations. This is also consistent with recent glider observations (Clement et al., 2023), which detected winter freshwater intrusions, plausibly arising from the Labrador Current. These intrusions have mesoscale and submesoscale origins and were previously identified starting from April only (Schmidt and Send, 2007). The increased freshwater flux to the central part of the Labrador Sea might disturb or even stop the deep convection (Straneo, 2006a), essential for the formation of fresh, cold, oxygenated and anthropogenic CO₂-laden LSW which then is exported to lower latitudes (Rhein et al., 2017; Koelling et al., 2022).

References

- Aagaard, K. and E. C. Carmack (1989). The role of sea ice and other fresh water in the Arctic circulation. *Journal of Geophysical Research* 94, pp. 14485–14498.
- Almansi, Matteo and Rien Gelderloos (2019). OceanSpy: A Python Package to Facilitate Ocean Model Data Analysis and Visualization. *Journal of Open Source Software* 4.38.
- Amante, C. and B.W. Eakins (2009). ETOPO1 1 Arc-Minute Global Relief Model: Procedures, Data Sources and Analysis. NOAA Technical Memorandum NESDIS NGDC-24.
- Appen, W.J. von, T.M. Baumann, M. Janout, N. Koldunov, Y.D. Lenn, R.S. Pickart, R.B. Scott, and Q. Wang (2022). Eddies and the distribution of eddy kinetic energy in the Arctic Ocean. *Oceanography* 35.3/4, pp. 42–51.
- Bailey, D.A., P.B. Rhines, and S. Häkkinen (2005). Formation and pathways of North Atlantic Deep Water in a coupled ice–ocean model of the Arctic–North Atlantic Oceans. *Climate Dynamics* 25, pp. 497–516.
- Brandt, P., F.A. Schott, A. Funk, and C.S. Martins (2004). Seasonal to interannual variability of the eddy field in the Labrador Sea from satellite altimetry. *Journal of Geophysical Research: Oceans* 109.C2.
- Chanut, J., B. Barnier, W. Large, L. Debreu, T. Penduff, J.M. Molines, and P. Mathiot (2008). Mesoscale eddies in the Labrador Sea and their contribution to convection and restratification. *Journal of Physical Oceanography* 38.8, pp. 1617–1643.
- Clement, C., E. Frajka-Williams, N. von Oppeln-Bronikowski, I. Gosczko, and B. de Young (2023). Cessation of Labrador Sea Convection by Freshening through (Sub)mesoscale Flows. *Journal of Physical Oceanography* 53.8, pp. 1959–1977.
- Cuny, J., P.B. Rhines, P.P. Niiler, and S. Bacon (2002). Labrador Sea boundary currents and the fate of the Irminger Sea Water. *Journal of Physical Oceanography* 32.2, pp. 627–647.

- Dickson, R.R., J. Meincke, S.A. Malmberg, and A.J. Lee (1988). The “great salinity anomaly” in the northern North Atlantic 1968–1982. *Progress in Oceanography* 20.2, pp. 103–151.
- Dukhovskoy, D.S., I. Yashayaev, A. Proshutinsky, J.L. Bamber, I.L. Bashmachnikov, E.P Chassignet, C.M. Lee, and A.J. Tedstone (2019). Role of Greenland freshwater anomaly in the recent freshening of the subpolar North Atlantic. *Journal of Geophysical Research: Oceans* 124.5, pp. 3333–3360.
- Eden, C. and C. Böning (2002). Sources of eddy kinetic energy in the Labrador Sea. *Journal of Physical Oceanography* 32.12, pp. 3346–3363.
- Fenty, I. and P. Heimbach (2013). Coupled sea ice–ocean-state estimation in the Labrador Sea and Baffin Bay. *Journal of Physical Oceanography* 43.5, pp. 884–904.
- Gelderloos, R., C.A. Katsman, and S.S. Drijfhout (2011). Assessing the roles of three eddy types in restratifying the Labrador Sea after deep convection. *Journal of Physical Oceanography* 41.11, pp. 2102–2119.
- Hoskins, B.J. (1974). The role of potential vorticity in symmetric stability and instability. *Quart. J. Roy. Meteor. Soc.* 100, pp. 480–482. doi: 10.1002/qj.49710042520.
- Katsman, C.A., M.A. Spall, and R.S. Pickart (2004). Boundary current eddies and their role in the restratification of the Labrador Sea. *Journal of Physical Oceanography* 34.9, pp. 1967–1983.
- Koelling, J., D. Atamanchuk, J. Karstensen, P. Handmann, and D. W. R. Wallace (2022). Oxygen export to the deep ocean following Labrador Sea Water formation. *Biogeosciences* 19, pp. 437–454.
- Lazier, J., R. Hendry, A. Clarke, I. Yashayaev, and P. Rhines (2002). Convection and restratification in the Labrador Sea, 1990–2000. *Deep Sea Research Part I: Oceanographic Research Papers* 49.10, pp. 1819–1835.
- Lilly, J.M., P.B. Rhines, F. Schott, K. Lavender, J. Lazier, U. Send, and E. D’Asaro (2003). Observations of the Labrador Sea eddy field. *Progress in Oceanography* 59.1, pp. 75–176.
- Lozier, M.S., F. Li, S. Bacon, F. Bahr, A.S. Bower, S.A. Cunningham, M.F. de Jong, L. de Steur, B. de Young, J. Fischer, and S.F. Gary (2019). A sea change in our view of overturning in the subpolar North Atlantic. *Science* 363.6426, pp. 516–521.

- Manucharyan, G. E. and A. F. Thompson (2017). Submesoscale sea ice-ocean interactions in marginal ice zones. *Journal of Geophysical Research: Oceans* 122.12, pp. 9455–9475.
- (2022). Heavy footprints of upper-ocean eddies on weakened Arctic Sea ice in marginal ice zones. *Nature Communications* 13.1, p. 2147.
- Marshall, J., A. Adcroft, C. Hill, L. Perelman, and C. Heisey (1997). A finite-volume, incompressible Navier Stokes model for studies of the ocean on parallel computers. *Journal of Geophysical Research: Oceans* 102, pp. 5753–5766.
- McGeehan, T. and W. Maslowski (2011). Impact of shelf–basin freshwater transport on deep convection in the western Labrador Sea. *Journal of Physical Oceanography* 41.11, pp. 2187–2210.
- Medium-Range Weather Forecasts, European Centre for (2011). ECMWF's Operational Model Analysis.
- Myers, P.G. (2005). Impact of freshwater from the Canadian Arctic Archipelago on Labrador Sea water formation. *Geophysical Research Letters* 32.6.
- Pennelly, C., X. Hu, and P. G. Myers (2019). Cross-isobath freshwater exchange within the North Atlantic subpolar gyre. *Journal of Geophysical Research: Oceans* 124.10, pp. 6831–6853.
- Pennelly, C. and P. G. Myers (2020). Introducing LAB60: A 1 / 60° NEMO 3.6 numerical simulation of the Labrador Sea. *Geoscientific Model Development* 13.10, pp. 4959–4975.
- Rhein, M., R. Steinfeldt, D. Kieke, I. Stendardo, and I. Yashayaev (2017). Ventilation variability of Labrador Sea Water and its impact on oxygen and anthropogenic carbon: a review. *Philosophical Transactions of the Royal Society A: Mathematical, Physical and Engineering Sciences* 375.2102, p. 20160321.
- Rieck, J.K., C.W. Böning, and K. Getzlaff (2019). The nature of eddy kinetic energy in the Labrador Sea: Different types of mesoscale eddies, their temporal variability, and impact on deep convection. *Journal of Physical Oceanography* 49.8, pp. 2075–2094.
- Schmidt, S. and U. Send (2007). Origin and composition of seasonal Labrador Sea freshwater. *Journal of Physical Oceanography* 37, pp. 1445–1454.

- Scoto, F., H. Sadatzki, N. Maffezzoli, C. Barbante, A. Gagliardi, C. Varin, P. Vallelonga, V. Gkinis, D. Dahl-Jensen, H.A. Kjær, and F. Burgay (2022). Sea ice fluctuations in Baffin Bay and the Labrador Sea during glacial abrupt climate changes. *Proceedings of the National Academy of Sciences* 119.44, e2203468119.
- Siegelman, Lia, Patrice Klein, Pascal Rivière, Andrew F. Thompson, Hector S. Torres, Mar Flexas, and Dimitris Menemenlis (2020). Enhanced upward heat transport at deep submesoscale ocean fronts. *Nature Geoscience* 13.1, pp. 50–55.
- Spall, M.A. (2004). Boundary currents and watermass transformation in marginal seas. *Journal of Physical Oceanography* 34.5, pp. 1197–1213.
- Straneo, F. (2006a). Heat and freshwater transport through the central Labrador Sea. *Journal of Physical Oceanography* 36.4, pp. 606–628.
- (2006b). On the connection between dense water formation, overturning, and poleward heat transport in a convective basin. *Journal of Physical Oceanography* 36.9, pp. 1822–1840.
- Tagklis, F., A. Bracco, T. Ito, and R.M. Castelao (2020). Submesoscale modulation of deep water formation in the Labrador Sea. *Scientific Reports* 10.1, p. 17489.
- Taylor, John R. and Raffaele Ferrari (2010). Buoyancy and wind-driven convection at mixed layer density fronts. *Journal of Physical Oceanography* 40.6, pp. 1222–1242.
- Taylor, John R. and Andrew F. Thompson (2023). Submesoscale Dynamics in the Upper Ocean. *Annual Review of Fluid Mechanics* 55, pp. 103–127.
- Thomas, L. N., A. Tandon, and A. Mahadevan (2008). Submesoscale Processes and Dynamics. *Geophysical Monograph Series*, pp. 17–38.
- Thomas, L. N., J. R. Taylor, R. Ferrari, and T. M. Joyce (2013). Symmetric Instability in the Gulf Stream. *Deep Sea Research Part II* 91, pp. 96–110.
- Thomas, M. D., A.-M. Treguier, B. Blanke, J. Deshayes, and A. Volodioire (2015). A Lagrangian Method to Isolate the Impacts of Mixed Layer Subduction on the Meridional Overturning Circulation in a Numerical Model. *Journal of Climate* 28, pp. 7503–7517.
- Thomson, R. E. and W. J. Emery (2014). Data Analysis Methods in Physical Oceanography. Newnes.

- Wang, Shihong, Zhenya Song, Weidong Ma, Qi Shu, and Fangli Qiao (2022). Mesoscale and submesoscale turbulence in the Northwest Pacific Ocean revealed by numerical simulations. *Deep Sea Research Part II: Topical Studies in Oceanography* 206, p. 105221.
- Yashayaev, I., M. Bersch, and H. M. van Aken (2007). Spreading of the Labrador Sea Water to the Irminger and Iceland basins. *Geophysical Research Letters* 34.10.

Acknowledgement

First, I want to thank my first supervisor Prof. Dr. Eleanor Frajka-Williams, for allowing me to write my master's thesis as part of the Experimental Oceanography group of the Institute of Oceanography. I appreciate the time and excellent advice she has given me over the last year. She gave me the possibility to gain a lot of insight into the world of physical oceanography.

Also, I would like to thank my second supervisor Dr. Louis Clement. His answers and support on my scientific and technical questions have helped me greatly improve my work.

I thank the Experimental Oceanography group for the nice atmosphere and interesting discussions at the weekly group meeting.

Special thanks to my girlfriend Tania for her understanding, love and moral support.

Eidesstattliche Versicherung

Hiermit versichere ich an Eides statt, dass ich die vorliegende Arbeit im Studiengang M.Sc. Ocean and Climate Physics selbstständig verfasst und keine anderen als die angegebenen Hilfsmittel – insbesondere keine im Quellenverzeichnis nicht benannten Internet-Quellen – benutzt habe. Alle Stellen, die wörtlich oder sinngemäß aus Veröffentlichungen entnommen wurden, sind als solche kenntlich gemacht. Ich versichere weiterhin, dass ich die Arbeit vorher nicht in einem anderen Prüfungsverfahren eingereicht habe und die elektronische Version der gedruckten entspricht.

Einer Veröffentlichung der vorliegenden Arbeit in der zuständigen Fachbibliothek des Fachbereichs stimme ich zu.

Hamburg, 12.03.2024 Unterschrift: 

den